Key Points:
- First account of eddies in the Western Arctic Ocean is presented based on satellite observations over open ocean and marginal ice zones
- Eddies range in size between 0.5 and 100 km and are ubiquitous over deep and shelf regions of the Western Arctic Ocean
- Cyclonic eddies are twice more frequent compared to anticyclones

Correspondence to:
I. E. Kozlov,
igor.eko@gmail.com

Eddies in the Western Arctic Ocean From Spaceborne SAR Observations Over Open Ocean and Marginal Ice Zones

Igor E. Kozlov[1,2] , Anastasia V. Artamonova[2], Georgy E. Manucharyan[3] , and Arseny A. Kubryakov[1]

[1]Marine Hydrophysical Institute of RAS, Sevastopol, Russia, [2]Satellite Oceanography Laboratory, Russian State Hydrometeorological University, Saint Petersburg, Russia, [3]California Institute of Technology, Pasadena, CA, USA

Abstract The Western Arctic Ocean is a host to major ocean circulation systems, many of which generate eddies that can transport water masses and corresponding tracers over long distances from their formation sites. However, comprehensive observations of critical eddy characteristics are currently not available and are limited to spatially and temporally sparse in situ observations. Here we use high-resolution spaceborne synthetic aperture radar measurements to detect eddies from their surface imprints in ice-free sea surface roughness, and in sea ice patterns throughout marginal ice zones. We provide the first estimate of eddy characteristics extending over the seasonally ice-free and marginal ice zone regions of the Western Arctic Ocean, including their locations, diameters, and monthly distribution. Using available synthetic aperture radar data, we identified over 4,000 open ocean eddies, as well as over 3,500 eddies in marginal ice zones from June to October in 2007, 2011, and 2016. Eddies range in size between 0.5 and 100 km and are frequently found over the shelf and near continental slopes but also present in the deep Canada Basin and over the Chukchi Plateau. We find that cyclonic eddies are twice more frequent compared to anticyclonic eddies at the surface, distinct from the dominating anticyclonic eddies observed at depth by in situ moorings and ice-tethered profilers. Our study supports the notion that eddies are ubiquitous in the Western Arctic Ocean even in the presence of sea ice and emphasizes the need for improved ocean observations and modeling at eddy scales.

Plain Language Summary Ocean eddies play an important role in the transport of heat, salt, and pollutants over long distances from their formation sites. However, their observations in the Arctic Ocean are complex due to severe weather and sea ice cover. Here we present results of high-resolution satellite observations over the ice-free ocean and in the marginal ice zones. Detailed eddy characteristics are for the first time presented for the Western Arctic Ocean. These results provide observational evidence that eddies are ubiquitous in this Arctic region even in the presence of sea ice and emphasize the need for improved ocean observations and modeling at eddy scales.

1. Introduction

Mesoscale eddies are commonly observed in the Arctic Ocean via field campaigns (D'Asaro, 1988; Hunkins, 1974; Padman et al., 1990; Pickart, 2004), from drifting ice-tethered profilers (Timmermans et al., 2008; Zhao et al., 2014, 2016) and moorings (Zhao et al., 2018; Zhao & Timmermans, 2015), as well as in microstructure observations in Canada Basin (Fine et al., 2018). Depending on their geographic location and depth in the water column, there is a multitude of possible eddy formation mechanisms in the Arctic including baroclinic and barotropic instabilities of mean flows including boundary currents (D'Asaro, 1988; Johannessen et al., 1993; Manley & Hunkins, 1985; Spall et al., 2008); convection-driven eddies in, for example, leads of polynyas (Muench et al., 2000); instabilities of outcropping surface fronts (Manucharyan & Timmermans, 2014); mixed layer instabilities of meltwater fronts (Lu, 2015; Manucharyan & Thompson, 2017); and wind-driven eddy formation over ice-edge boundaries (Johannessen et al., 1987). A recent analysis of drifter observations in the Beaufort Sea indicates the evidence of intense submesoscale dynamics driving enhanced lateral and vertical fluxes in the Arctic Ocean mixed layer (Mensa et al., 2018). Since mesoscale and submesoscale eddies play a key role in transporting water masses, inducing isopycnal and vertical transport of salt, heat, and nutrients, they are not only tightly linked to the dynamics of large-scale flows like the Beaufort Gyre (Manucharyan et al., 2016; Manucharyan & Spall, 2016; Meneghello et al., 2017) but also affect biogeochemical cycles including phytoplankton blooms (Abraham et al., 2000; Niebauer & Smith, 1989; Watanabe et al., 2014).
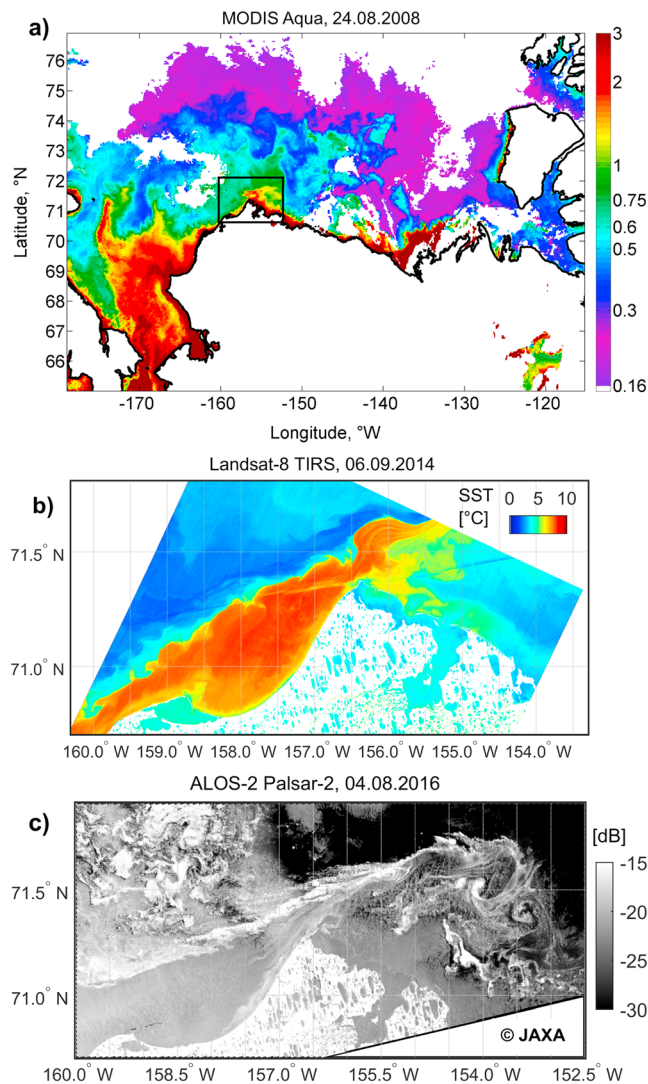
Figure 1. Map of study site with examples of eddy manifestations in (a) medium-resolution eight-day composite chlorophyll *a* map derived from visible band MODIS Aqua data on 24 August 2008, and two high-resolution images showing the generation of numerous eddies over the unstable Alaskan Coastal Current jet passing Point Barrow in (b) thermal infrared Landsat-8 SST image taken on 6 September 2014 and (c) ALOS-2 Palsar-2 image taken on 4 August 2016. © NASA ©USGS © JAXA

Mesoscale eddy-resolving numerical modeling of the Arctic Ocean are computationally demanding due to relatively small Rossby deformation radii, which is O(1 km) over low-stratified and shallow shelfs and O(10 km) in deeper basins (Nurser & Bacon, 2014). As a result, most of the climate projection models are not eddy-resolving, implementing eddy parameterizations that were not validated for the Arctic Ocean. Nonetheless, a few eddy-resolving global ocean models (e.g., LLC4320 model; Rocha et al., 2016; Su et al., 2018), pan-Arctic simulations, and regional models (Hattermann et al., 2016; Wekerle et al., 2017) have been developed to explicitly simulate eddy dynamics, demonstrating their critical role in transporting heat and salt anomalies across major currents. However, validating these high-resolution models requires not only climatological observations but also statistical information about eddies, which is currently very limited. In addition, these computationally demanding simulations can only be run for short periods of time (years to a decade) being more appropriate for process studies rather than for constructing ocean state estimates or making long-term predictions.

While providing a framework for revealing critical processes and testing dynamical hypotheses, eddy-resolving models as well as in situ observations in the Arctic are limited in either temporal or spatial domain, suggesting the use of satellite data for obtaining a comprehensive coverage. However, conventional utilization of available satellite observations in the Arctic to infer surface ocean characteristics such as dynamic height, temperature, and salinity is complicated by the presence of sea ice and the relatively small size of mesoscale eddies. Satellite observations of ocean dynamic height supported major thrusts in our understanding of mesoscale eddies and their interactions with large-scale currents (Arbic et al., 2013; Wunsch & Stammer, 1998). The altimetry revealed mesoscale eddy field at a resolution of O(100 km) in the world ocean (Chelton et al., 2011), including the coastal ocean and semienclosed seas (e.g., Kubryakov & Stanichny, 2015) but its coverage most often lacks polar oceans. Recently developed under-ice dynamic topography data (Armitage et al., 2016) provided a great value for monitoring the large-scale circulation but its monthly temporal resolution and 25-km grid do not resolve eddies. Moreover, since the Arctic eddies are several times smaller in size than low-latitude eddies, the satellite altimetry even in ice-free regions could only resolve a small fraction of the eddies, leaving the Arctic Ocean essentially unobserved at its mesoscales and below.

Spatial information on eddy field in the Arctic Ocean is sometimes available from medium- and high-resolution satellite data in visible and infrared bands. Such data sets may show very distinct signatures of eddy formation over shallow coastal areas and over a deep basin owing to, for example, spatial redistribution of chlorophyll *a* concentration (Figure 1a). Eddies of various scales also modulate the thermal structure of the upper ocean and, therefore, are well visible in remotely sensed images acquired in thermal infrared bands. This is well exemplified in a high-resolution Landsat-8 sea surface temperature map produced using the algorithm from (Aleskerova et al., 2017) and showing generation of numerous small-to-mesoscale eddies over the unstable Alaskan Coastal Current jet before passing Point Barrow (Figure 1b). However, such data are very rare due to intensive cloud cover in the Arctic Ocean. In turn, active microwave sensing techniques having all-weather and frequent sampling capabilities, and high spatial resolution (10–100 m) are critical for observing mesoscale and submesoscale upper ocean processes in the Arctic. This is exactly what spaceborne synthetic aperture radars (SARs) can provide, as is well illustrated in Figure 1c showing dozens of eddies formed in the turbulent wake of the Alaskan Coastal Current jet east from Point Barrow. Notably, eddy

Table 1

Number of Spaceborne SAR Images Used for Eddy Detection in the Western Arctic Ocean

Year	Sensor	June	July	August	September	October	Total
2007	ASAR	11	23	57	38	18	147
2011	ASAR	83	59	32	34	17	225
2016	S-1 A, B	30	58	52	27	17	184
2016	Palsar-2	-	-	8	17	11	36
Total							**592**

signatures are formed here due to entrainment of sea ice into the current jet from the adjacent marginal ice zones (MIZ) located north-west from Point Barrow when the floating ice fully mimics the ocean circulation regime in this region.

Indeed, SAR images taken from space proved to be an effective tool for observing various upper ocean circulation features like eddies and fronts over the ice-free ocean regions (Atadzhanova et al., 2017; Johannessen et al., 1996, 2005; Kozlov et al., 2012; Kudryavtsev et al., 2014) and in the marginal ice zone (Johannessen et al., 1987; Shuchman et al., 1987). Primarily, it is a modulation of short-scale surface roughness patterns due to wave-current interactions, accumulation of slicks or drifting ice floes, and near-surface wind variation across oceanic fronts that make eddy features well visible in spaceborne SAR images (Johannessen et al., 1996, 2005). Eddies often manifest in the form of spirals (Eldevik & Dysthe, 2002) associated with streaks of strong cyclonic shear and convergence formed by shear instability due to variations in the larger-scale coastal currents (Johannessen et al., 1993). In the marginal ice zones, cyclonic eddies and filaments tend to accumulate the sea ice and anticyclonic flows repel the sea ice (Manucharyan & Thompson, 2017), explaining the formation of eddy-like structures in sea ice concentration patterns seen in SAR images. The accumulation of sea ice in a cyclonic filament was also observed during an observational campaign in Fram Strait (Von Appen et al., 2018). Thus, SAR snapshots often contain strong signatures of ocean eddies and can be used for their detection. While SAR data have already been used to study eddies over certain Arctic regions (Atadzhanova et al., 2017; Johannessen et al., 1987; Mensa et al., 2018), the use of such data is still rather limited and comprehensive eddy observations spanning the vast regions of the Arctic Ocean are lacking.

In this paper, we analyze high-resolution spaceborne SAR measurements to provide the first detailed spatial picture of eddy properties in the Western Arctic Ocean. Data and methods for detecting and characterizing the eddies are introduced in section 2. In section 3, we present the results of eddy detection and their properties over ice-free ocean regions and in marginal ice zone from high-resolution SAR observations. In section 4, we summarize and discuss our results in the context of past and ongoing studies.

2. Materials and Methods

In this study, we use multimission spaceborne SAR observations of eddy signatures in the Western Arctic Ocean. The data of each of the SAR sensors and methods used for eddy detection are described in subsections below.

2.1. SAR Data

Here we analyze archived C-band SAR images acquired by the European Space Agency Envisat Advanced SAR (ASAR) instrument in June–October 2007 and 2011, as well as data from currently operating SAR missions—Copernicus Sentinel-1A, -1B SAR-C instruments working in C-band, and Japanese L-band ALOS-2 PALSAR-2 instrument operated by Japan Aerospace Exploration Agency. The SAR imagery from the latter two was exploited for the period from June to October 2016. A summary of the SAR data used in the analysis is presented in Table 1.

Envisat ASAR data used in the analysis were obtained from the European Space Agency's rolling archive. These ASAR images were Wide Swath mode with 150-m spatial resolution. In total, 372 ASAR images were analyzed with 147 images acquired in 2007 and 225 images in 2011 (Table 1). Sentinel-1A, -1B data were obtained from Copernicus Open Access Hub (https://scihub.copernicus.eu). These were high- and medium-resolution Ground Range Detected images taken in Interferometric Wide swath and Extra-Wide swath modes with a spatial resolution of about 20 and 90 m, respectively. In total, 184 Sentinel-1A and 1B SAR images were analyzed during June–October 2016. To enhance the data coverage in August–October 2016, 36 ALOS-2 PALSAR-2 images were additionally obtained from Japan Aerospace Exploration Agency. These L-band SAR images were acquired in Scan SAR nominal, Fine, and Ultra-fine modes with a spatial resolution of 50, 12.5, and 5 m, respectively. In total, 592 SAR images were used in the analysis.
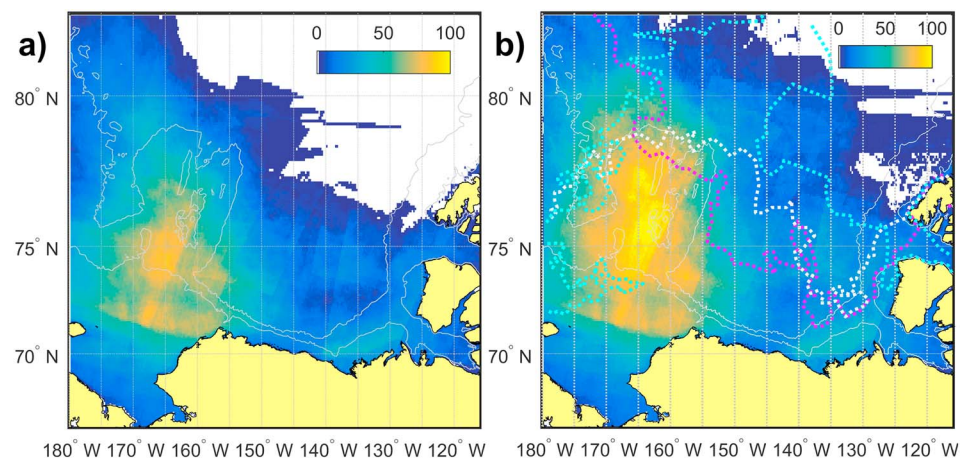
Figure 2. Spatial coverage of the study site by SAR data during three extended summer seasons in 2007, 2011, and 2016 for (a) open-water regions only and (b) including the marginal ice zone. Dotted lines in (b) show 15% ice concentration for 1 September 2007 (magenta), 2011 (white), and 2016 (cyan). The number of available SAR images is shown in color. Grey lines indicate the 200- and 2,000-m isobaths taken from IBCAO v.3.0.

Analysis of historical ASAR data was performed using Matlab-based software suggested in Kozlov et al. (2015), while the analysis of Sentinel-1 and Palsar-2 data was done using the open-source European Space Agency SNAP software (http://step.esa.int/main/toolboxes/snap/). The entire procedure of data preprocessing and eddy detection was similar for all the data. The original SAR data were first calibrated to normalized radar cross-section units, then normalized to remove the signal trend in the range direction, and finally smoothed to reduce the speckle noise using either the adaptive Wiener filter (Lim, 1990) in Matlab, or a Lee filter (Lee, 1983) incorporated to the SNAP software. Ice masking was done using daily AMSR-E and its successor AMSR-2 sea ice concentration maps produced by the University of Bremen (Spreen et al., 2008). To account for eddies near the ice edge and in the marginal ice zone (defined here as a region with 15%–80% ice concentration), the regions with sea ice concentration below 80% were considered.

Figure 2 shows maps of the spatial coverage of the study site by SAR data when considering only open-water regions in each SAR scene (Figure 2a) and including marginal ice zone (Figure 2b) during three extended summer seasons in 2007, 2011, and 2016. As seen, the resulting data coverage maps are not spatially homogeneous and have a clear west-east asymmetry due to different ice season length in the Chukchi and Beaufort Seas. A higher number of effective SAR observations (up to 80–100 SAR looks) is available for the western part over the northern Chukchi Sea. The SAR coverage is also somewhat higher and extends further north for the MIZ (Figure 2b).

2.2. Manifestation and Detection of Eddies in SAR Images

As mentioned above, eddies can be manifested in SAR images owing to several different mechanisms: (i) interaction of short wind waves with eddy-induced varying surface currents, (ii) accumulation of surfactant films in surface current convergence zones associated with eddy orbital motion, (iii) wind stress changes over oceanic temperature fronts, and (iv) spatial redistribution of drifting ice tracing the upper ocean circulation features.

In the first case, eddy-induced surface current gradients modulate the energy of short wind waves resulting in the generation of enhanced (suppressed) surface roughness patterns along the surface current convergence (divergence) zones. The SAR signal is sensitive to such surface roughness variations and, under moderate-to-fresh winds, local current fronts with strong convergence and divergence at the surface are manifested in SAR as alternating bright and dark patterns, respectively (Johannessen et al., 2005; Kudryavtsev et al., 2014). An example of this mechanism at work is shown in Figure 3a, where a street of spiral cyclones with a diameter of about 4–6 km is clearly seen. Under low winds (up to 5 m/s), the manifestation patterns will substantially change in presence of surfactant films that would tend to accumulate at surface current convergence zones making eddy boundaries appear dark in SAR images (Figure 3b).
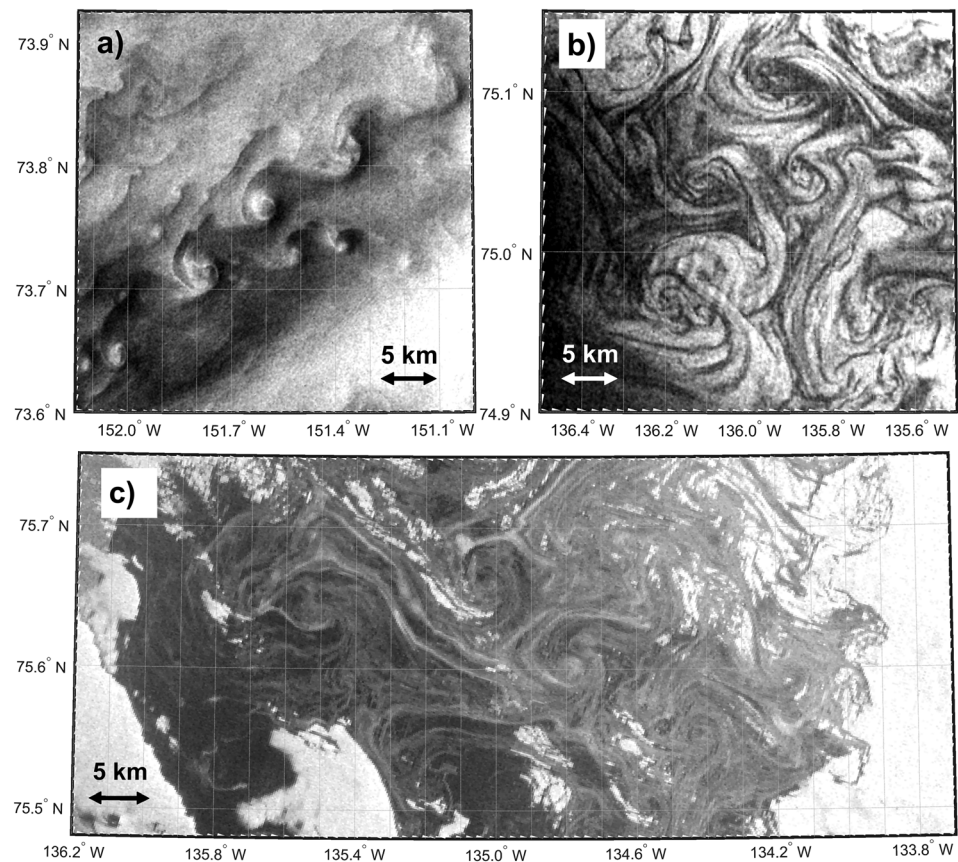
Figure 3. Examples of eddy manifestation and detection in ALOS-2 Palsar-2 images owing to different mechanisms: (a) wave-current interactions (20 September 2016, 22:56 UTC), (b) accumulation of natural films in surface current convergence zones (21 September 2016, 21:40 UTC), and (c) floating ice fields in the marginal ice zone (27 September 2016, 22:07 UTC). © JAXA

Local variation of surface wind stress, resulting from the transformation of the marine atmospheric boundary layer stratification across the temperature fronts, is another mechanism for eddy manifestation in SAR images, provided that eddy-trapped water has pronounced sea surface temperature anomaly relative to ambient waters. In such case, suppression (enhancement) of wind stress over cold (warm) sector of the front results in a pronounced decrease (increase) of radar backscatter and formation of dark (bright) patterns in SAR images relative to the background. This mechanism is also present in Figure 3a, where the radar signal over a set of cyclones is clearly below (darker) than that of ambient waters.

The last and one of the most prominent mechanisms of eddy manifestation in SAR images of polar oceans is that attributed to drifting ice floes either near the ice edge or within the marginal ice zone (Figure 3c). As pointed out by Shuchman et al. (1987), under light to moderate wind conditions the morphology of the marginal ice zone reflects the underlying ocean circulation features. Figure 3c shows an example of a SAR image with this mechanism at work.

Upon the preprocessing step, every image was visually inspected at full resolution in search of eddy signatures described above and exemplified in Figure 3. Then by looking at eddy boundaries outlined due to accumulation of slicks, floating ice, or enhanced wave breaking, their location, diameter, vorticity sign, and manifestation type were defined manually, similarly as what was done, for example, in Dokken and Wahl (1996), Karimova (2012), Karimova and Gade (2016), and Atadzhanova et al. (2017). All detected eddies were then split into two major groups—those identified over open-water regions (hereinafter, open-water (OW) eddies) and eddies manifested owing to spatial redistribution of drifting ice floes near the ice edge and in the marginal ice zone (hereinafter, MIZ eddies). Mean values of various eddy properties were then defined on a horizontal grid of 30 × 40 cells with an average cell size of 50 × 50 km. Depth values corresponding to

Table 2

Summary of Open-Water Eddy Detection in Spaceborne SAR Data in the Western Arctic Ocean in June–October 2007, 2011, and 2016

Year	2007		2011		2016		All years	
Month	C^1	AC^2	C	AC	C	AC	C	AC
June	13	5	0	0	0	0	13	5
July	222	170	23	7	0	0	245	177
August	489	231	33	7	476	160	998	398
Sept	85	31	71	21	824	321	980	373
October	0	1	15	5	520	348	535	354
Total	809	438	142	40	1820	829	**2771**	**1307**
		1247		182		2649		**4078**

C^1 denotes cyclonic eddies, while AC^2 anticyclonic ones.

eddy coordinates were then retrieved from IBCAO version 3.0 (Jakobsson et al., 2012). The human supervised method could contain various biases in eddy identification which could be diminished upon further automatization of the eddy detection methodology. However, to our knowledge, such methods are not readily available for the analysis of multimission spaceborne SAR data. Nonetheless, our method did result in a large number of identified eddies and allow to build up the first comprehensive estimate of eddy properties in the Western Arctic Ocean.

3. Results of Spaceborne SAR Observations

Tables 2 and 3 give a summary of eddy detection results obtained upon the processing of all available SAR images. Altogether 7,749 eddies were identified during three extended summer seasons from SAR observations with 4,078 eddies detected in open-water regions (Table 2) and 3,671 eddies in the marginal ice zone and near the ice edge (Table 3).

We should note here that in case of subsequent SAR images and long-living eddies, the same eddy can be potentially counted several times in our record. Moreover, the total number of detected eddies clearly depends on the number of the used SAR images (and hence the observed areas of OW and MIZ regions) that varies a lot from month to month and year to year.

To reduce these effects, below we provide the normalized eddy numbers that are obtained by normalizing the absolute eddy numbers presented in Tables 2 and 3 by the corresponding number of SAR observations of the ice-free/MIZ regions for a given month (Figure 4).

The most prominent feature of the obtained results is that cyclonic eddies strongly dominate over anticyclones. Surprisingly, this is true both for OW and MIZ eddies (see Tables 2 and 3). A general rule for all months and years is the mean ratio of 65–70% of cyclonic eddies versus 30–35% of anticyclones. At the same time, a big portion of eddies was observed in the form of mushroom-like eddy dipoles with a cyclonic vortex going in pair with an anticyclonic one.

For OW eddies, most of them were detected in August and September (Table 2) when the region has a minimum ice cover extent. Nevertheless, October 2016 is also remarkable for a high number of OW eddies detected, while only a few of them were identified in October 2007 and 2011. A similar result is obtained for July when a lot of eddies were detected in 2007, and very few or none of them were detected in 2011 and 2016, respectively. The lowest number of eddy occurrences is clearly found in June, when the ice cover extent is still well above its minimum.

As seen from Table 2 and Figure 4a, the number of OW eddies observed for a given month strongly varies depending on the particular year. In 2007, the number of OW eddies clearly peaks in August, while the normalized numbers shown in Figure 4a have a maximum value in June and constantly decrease toward October. Such relatively high normalized eddy numbers in June and July 2007 in fact are caused by small number of the ice-free SAR images during these months as compared to August–October 2007. In 2011, the overall level of eddy activity is rather low and nearly constant between July and October (Figure 4a). A very pronounced monthly variability of the normalized eddy numbers is seen in 2016. Although a certain amount of the ice-free SAR images was available for June and July 2016 (Table 1), no OW eddies were detected in these data. In contrast, a record maximum value is obtained in August 2016, and then it gradually decreases in September and October 2016.

According to observations, MIZ eddies also have a distinct seasonal cycle (see Table 3 and Figure 4b). When looking to the absolute eddy numbers, the monthly variability of MIZ eddies is rather similar to that of OW eddies (compare numbers in Tables 2 and 3). The maximum of their occurrences is recorded in September (44%) when marginal ice zone is well developed, while August and October have second (30%) and third

Table 3

Summary of MIZ Eddy Detection in Spaceborne SAR Data in the Western Arctic Ocean in June–October 2007, 2011, and 2016

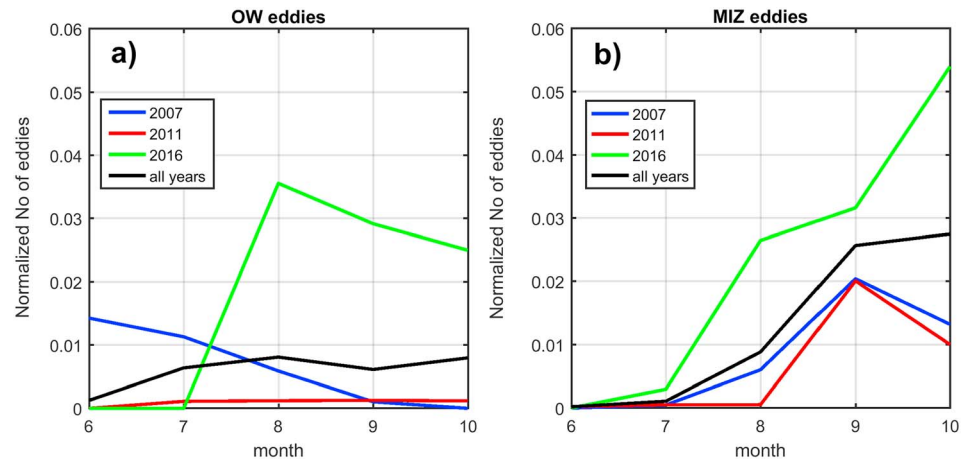| Year	2007		2011		2016		All years	
Month	C	AC	C	AC	C	AC	C	AC
June	0	0	2	2	0	0	2	2
July	9	4	10	9	36	21	55	34
August	159	173	11	11	497	254	667	438
Sept	121	67	295	170	603	344	1019	581
October	127	37	53	23	381	252	561	312
Total	416	281	371	215	1517	871	**2304**	**1367**
		697		586		2388		**3671**

Figure 4. Monthly variability of the normalized number of (a) open-water and (b) MIZ eddies detected in June–October 2007 (blue), 2011 (red), and 2016 (green).

(24%) numbers in the record. However, the normalized values show slightly different pattern (Figure 4b). All years are marked by constantly rising numbers from the beginning of summer toward September with the highest values and the most rapid rise observed in 2016. The years of 2007 and 2011 have their peaks in September as well, but October values now exceed those of August (compare with absolute numbers given in Table 3). In 2016, the maximum of the normalized number of eddies is found in October.

Considering the interannual variability of eddy occurrences, the highest absolute number of OW eddies was identified in 2016. It counts for 2,649 open-water eddies (65% of all OW eddies), which is twice higher than was observed in 2007 and 2011 together. In turn, the year of 2011 has the lowest record counting only for 182 OW eddies versus 1,247 eddies identified in 2007. When looking to the normalized values, the difference between 2007 and 2011 becomes less pronounced but still significant, while the number of eddies in 2016 is 5 times higher than a sum of those for 2007 and 2011. The latter clearly indicates a more intensive generation of OW eddies in 2016 as compared to 2007 and 2011.

For MIZ eddies, the year of 2016 also has the highest absolute number of eddies identified in the MIZ and near the ice edge. Yet their numbers are rather similar in 2007 and 2011 with slightly more MIZ eddies detected in 2007 (Table 3). Normalized values confirm the above results and show much higher number of MIZ eddies detected in July–October 2016 (Figure 4b).

Figure 5 shows the locations of eddies found in 2007, 2011, and 2016 over open-water regions. Blue and red circles mark cyclonic and anticyclonic eddies, respectively. Due to longer and more persistent ice cover in the north, OW eddies are predominantly found in the southern and central parts of the study region with many of them detected over shallow shelfs, shelf breaks, and continental slopes. However, about 13% (523 eddies) were found north of 75°N extending up to 80.17°N (not shown in Figure 5). Notably, OW cyclones and anticyclones are often found over the same locations emphasizing that many of them comprise eddy dipoles, as already noted above.

As seen in Figure 5a, eddy locations nicely mark the main pathways of the Pacific water crossing the Chukchi Sea. A very dense eddy pattern is found along the Alaskan Coastal Current going toward the Barrow Canyon where it splits and continues northwest along the shelf break to the Chukchi Sea and eastward along the entire shelf break region in the southern Beaufort Sea. The total number of eddies identified over these regions exceeds 50 eddies per grid cell (equal to about 50 × 50 km; Figure 5b). A large number of eddies is also found in the vicinity of Mackenzie River Delta, west of Banks Island, and in the eastern part of the Amundsen Gulf. Apart of shelf and shelf break regions, about half of all OW eddies are identified over the deeper Chukchi Plateau and the Beaufort Gyre regions peaking over depths of 3,000–4,000 m (Figure 7a). Several locations with a high number of eddies are seen along the southern rim of the Beaufort Gyre.

Figure 5c shows a map of a relative observational frequency (ROF) of OW eddies defined as a ratio between the total number of eddies encountered within a given grid cell (Figure 5b) and the number of ice-free SAR looks of that cell (Figure 2a). In fact, it is very similar to the map shown in Figure 5b, and the locations with a
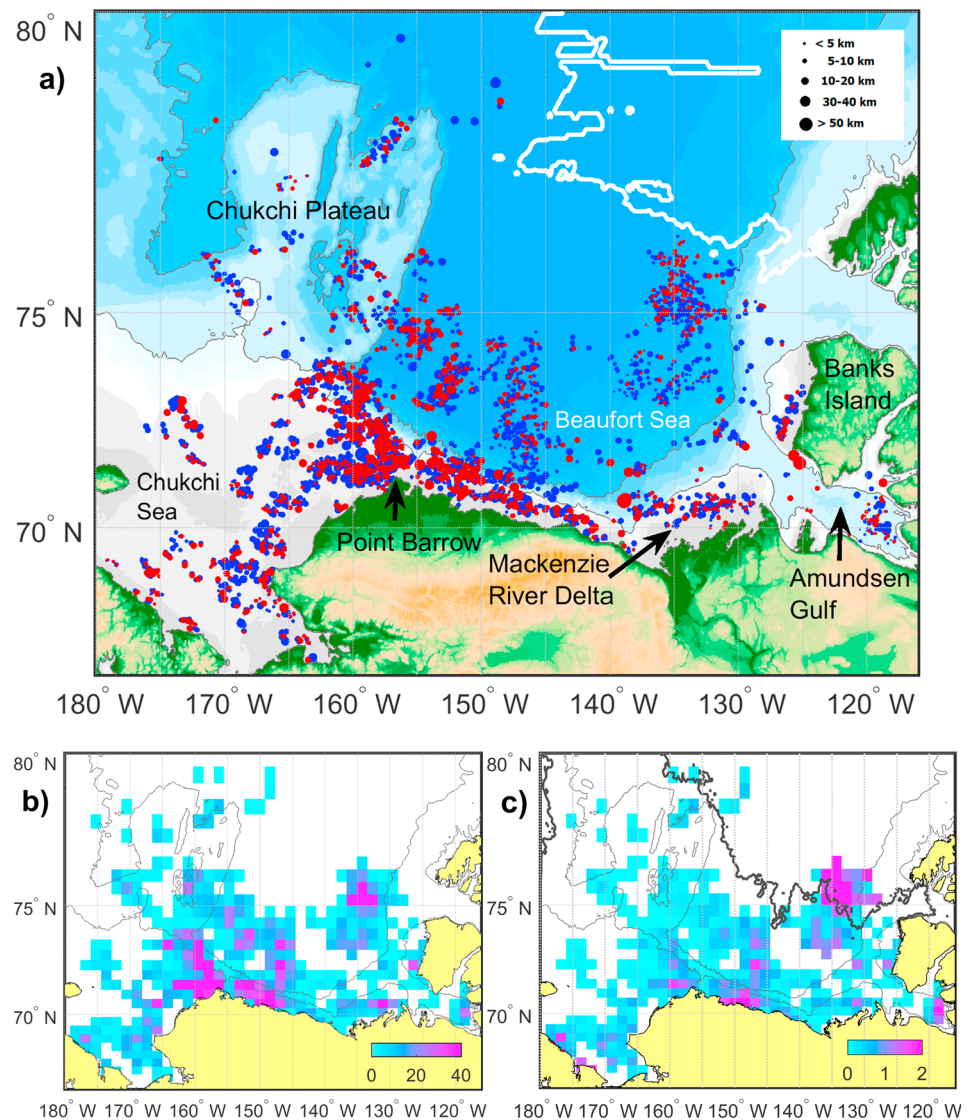
Figure 5. (a) Locations, (b) the total number, and (c) the probability of open-water eddies identified using the satellite SAR data in June–October 2007, 2011, and 2016. Blue (red) circles in (a) mark cyclonic (anticyclonic) eddies. Marker size is proportional to eddy diameters. The white line in (a) denotes the boundary of a region where no ice-free SAR data were available. The thick black line in (c) denotes the boundary of a region with the number of ice-free SAR images below 10. Overlaid are the 200- and 2,000-m isobaths taken from IBCAO v.3.0.

high total number of eddies are characterized by ROF values of 1–2 (maximum 11). This either means that every ice-free SAR image always captures 1–2 (maximum 11) eddies in that location, or more eddies are detected at once but less frequently. The thick black line in Figure 5c marks a boundary beyond which the total number of ice-free SAR looks is below 10, for example, is very low compared to the maximum value of nearly hundred SAR images in some other regions (see Figure 2b for reference). As seen, one of major eddy hot spots (centered at 76°N, 134°W) is located beyond this boundary (north of it) because it was ice-free only for a couple of weeks in late August to early September 2016. Yet even a short ice-free period of that region enabled to reveal a very strong eddy activity with over a hundred eddies detected by SAR. The peak value of OW eddy ROF histogram (not shown) is about 0.2, equivalent to observing just one eddy within a grid cell in every fifth SAR image.

Figure 6 provides details about the spatial distribution of MIZ eddies identified throughout the study period. As seen in Figure 6a, MIZ eddies are spread more homogeneously over the entire study domain as compared to OW eddies due to seasonal development and migration of the marginal ice zone. They extend from 68.9°N
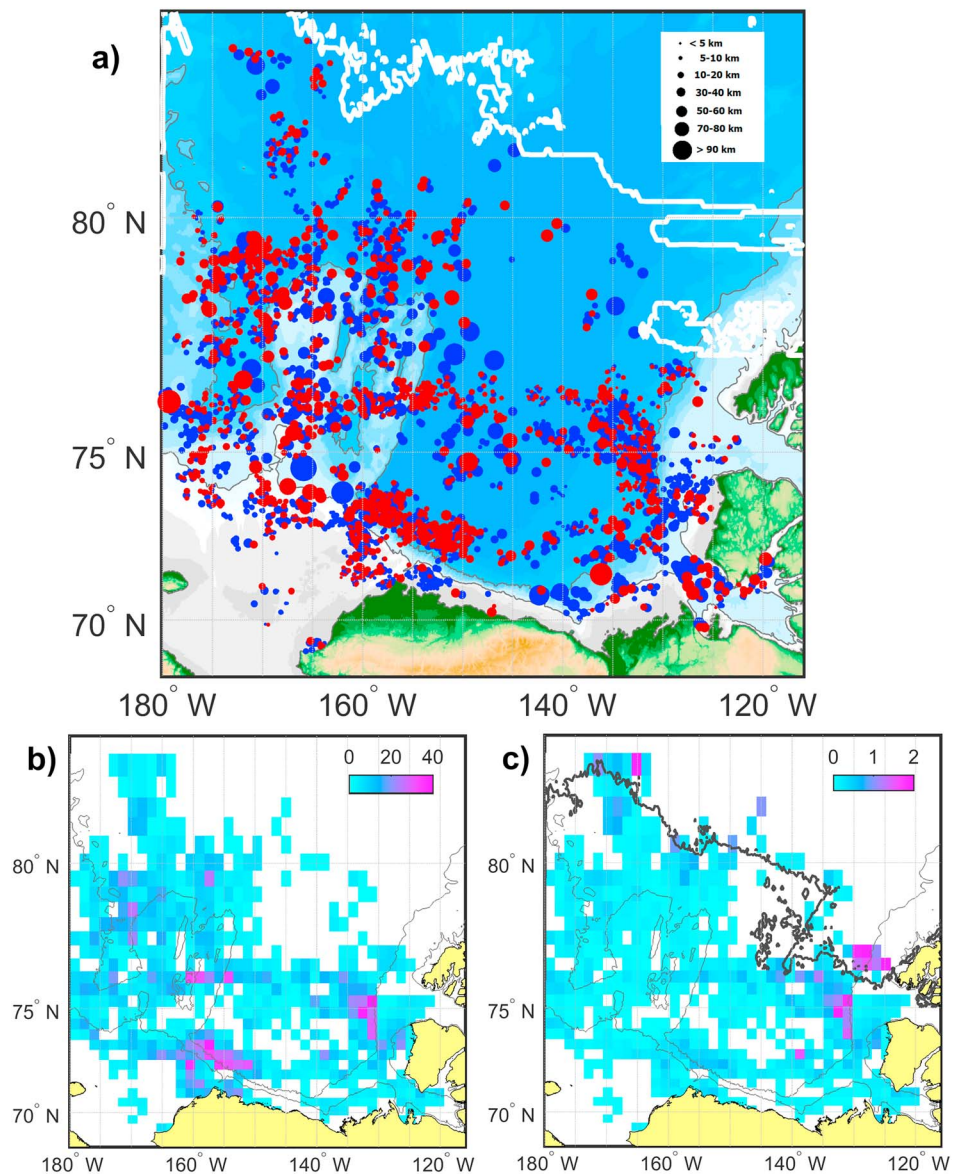
Figure 6. Same as Figure 5 but for MIZ eddies. The white line in (a) shows the boundary north of which no SAR observations over the MIZ regions were available.

up to 84.4°N, while about 54% of all MIZ eddies are found west from Point Barrow (156.2°W). Yet some locations with a higher number of MIZ eddies might be noted in Figure 6b. Many of them were observed over the continental slope at the boundary between the Chukchi and Beaufort Seas, in the eastern part of the Beaufort Gyre centered at 75°N, 132°W, and in different locations between the Mendeleev Ridge and the Chukchi Plateau, and further north (Figure 6b). One may also note that, in general, MIZ eddies are somewhat larger in size than OW eddies (see more details in Figure 9).

The highest value of relative observational frequency for MIZ eddies (>1) is found in the eastern part of the Beaufort Gyre, as well as in some other locations in the north where the overall number of SAR observations was not high (see the position of the thick black line in Figure 6c). The mean ROF value for MIZ eddies found over the most part of the study domain is about 0.1–0.2. Such relatively low values might be attributed to the fact that over particular locations such type of eddies can be observed only when the MIZ exists there. This is illustrated in Figure 7 showing seasonal changes in the latitude of MIZ eddies from July to November. As seen, MIZ eddies are observed within a narrow band of latitudes centered at 71°N at the beginning of ice
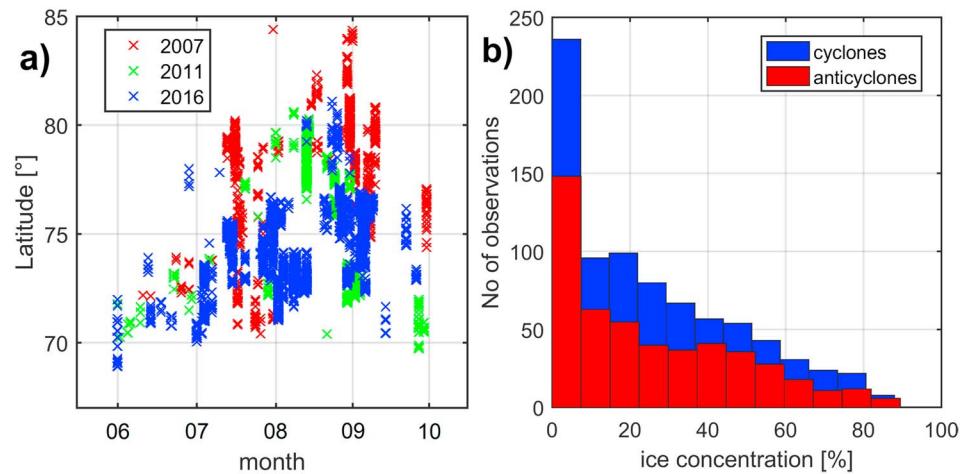
Figure 7. (a) Seasonal changes in latitudinal position of MIZ eddies from July to November. Red, green, and blue crosses mark the locations of eddies identified in 2007, 2011, and 2016, respectively. (b) Histogram distribution of the number of observed MIZ eddies as a function of sea ice concentration.

melt season in July, identically for all years (Figure 7). During the season, mean latitudes gradually rise, the latitudinal band widens, and spans 5–7° of latitude peaking in late September at 81°N in 2016 (blue crosses in Figure 7) and at 84.4°N in 2007 and 2011 (red crosses in Figure 7). A rapid decrease of latitudes down to 70°N is then observed during October. Figure 7b shows a histogram distribution of the number of MIZ eddies as a function of sea ice concentration. In general, the number of eddies clearly depends on sea ice concentration with more eddies detected over less ice-covered waters.

The distribution is dominated by one sharp mode around 0–10% ice concentration originating from eddies observed along the ice edge. The shape of distribution is nearly identical for cyclones and anticyclones, yet a small blurred mode around 20% ice concentration is also observed for cyclones.

Figure 8 shows histogram distributions of the number of eddies as a function of total water depth corresponding to the location of eddies in open-water (Figure 8a) and in the marginal ice zone (Figure 8b). As seen, cyclonic and anticyclonic OW eddies have two similar peaks—the first one is found over 20–100-m depths (42% of all OW eddies), while the second one is found over 1,500–4,000-m depths (38%). Interesting to note, the number of eddies found over shallow shelfs (<200 m) and deep waters (200–4,000 m) is equal. MIZ eddies have a similar range of depth values (Figure 8b), yet about 70% of these eddies are found over the depths exceeding 1,000 m with a mean depth of about 2,000 m.
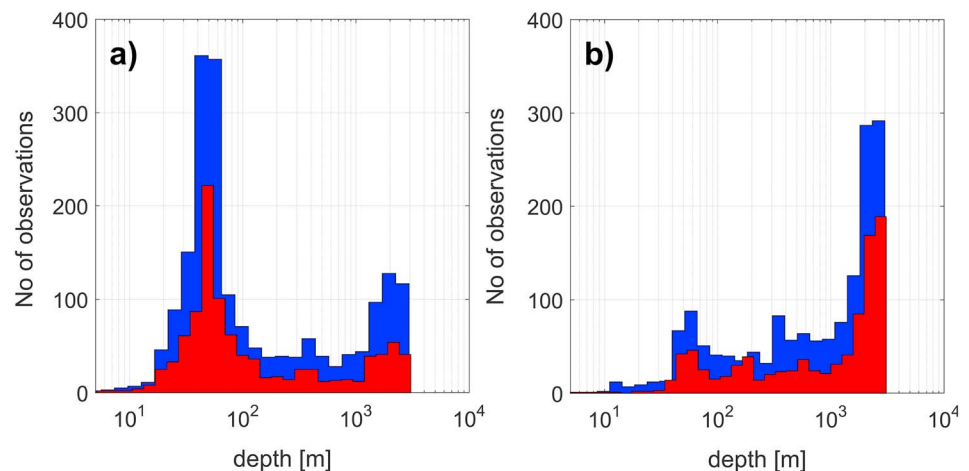

Figure 8. Histogram distributions of the number of eddies as a function of total water depth corresponding to the eddy locations in (a) the open water and (b) in the MIZ. Blue and red colors mark cyclonic and anticyclonic eddies, respectively.
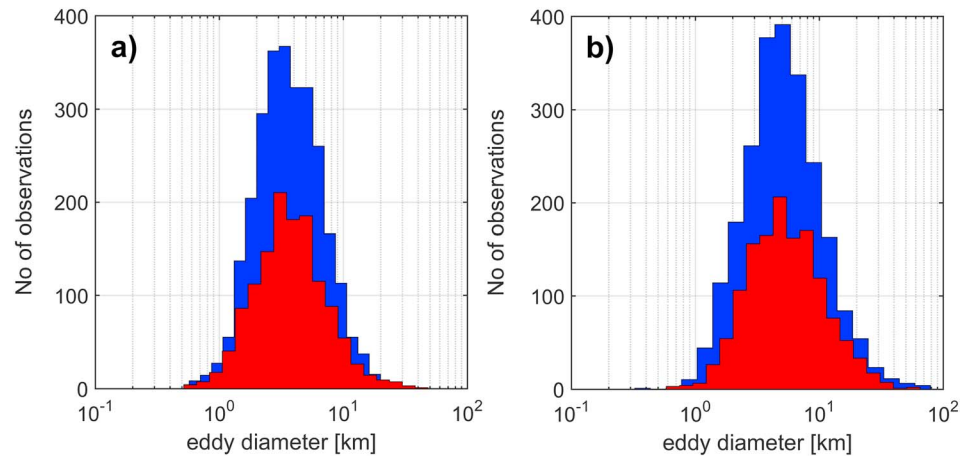
Figure 9. Histogram distributions of the number of eddies as a function of eddy diameter for eddies identified over (a) the open water and (b) in the MIZ. Blue and red colors mark cyclonic and anticyclonic eddies, respectively.

Histogram distributions of the number of eddies as a function of eddy diameters for the open water and the MIZ are shown in Figure 9. The range of diameters for open-water eddies is from 0.5 to 61 km. However, diameter values of about 94% of OW eddies do not exceed 10 km with a mean value of 4.7 km. For MIZ eddies, the range of diameters is wider, from 0.3 to 106 km, and the mean value is also higher being 6.8 km. Larger MIZ eddies with diameters over 10 km were observed in 17% of cases (634 eddies). As observed
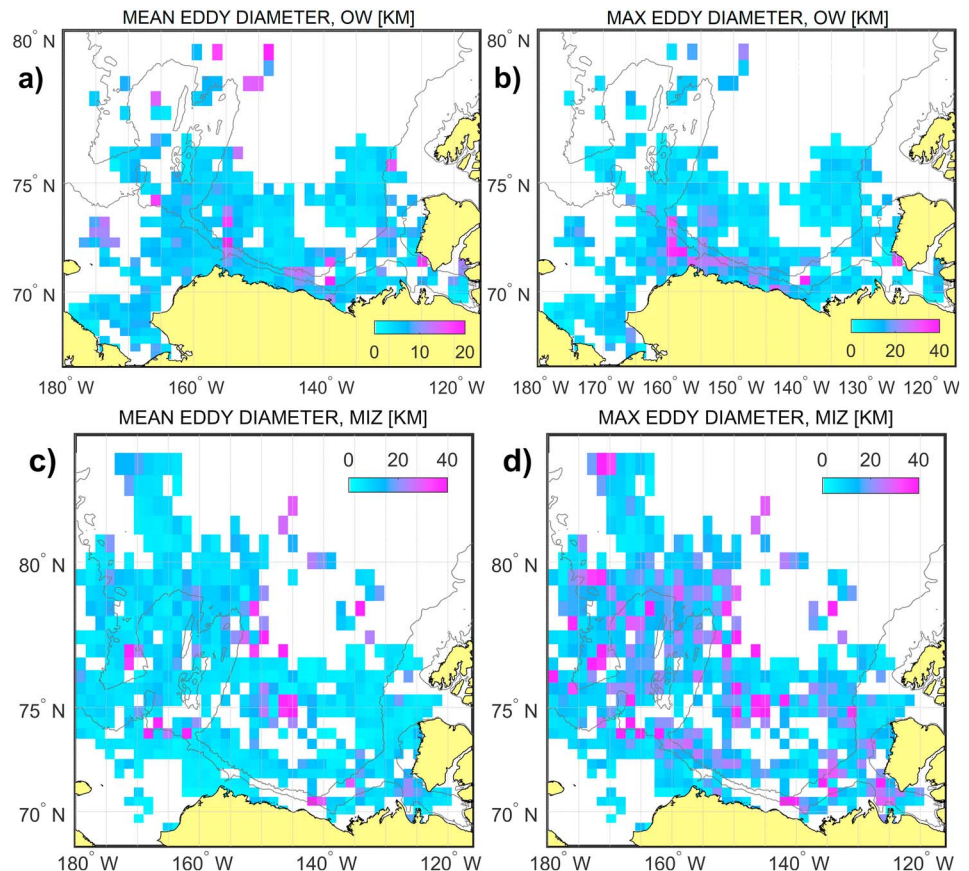

Figure 10. Spatial distribution of (a and c) the mean and (b and d) the maximum eddy diameters for eddies found in the open water (a and b) and over the MIZ (c and d).
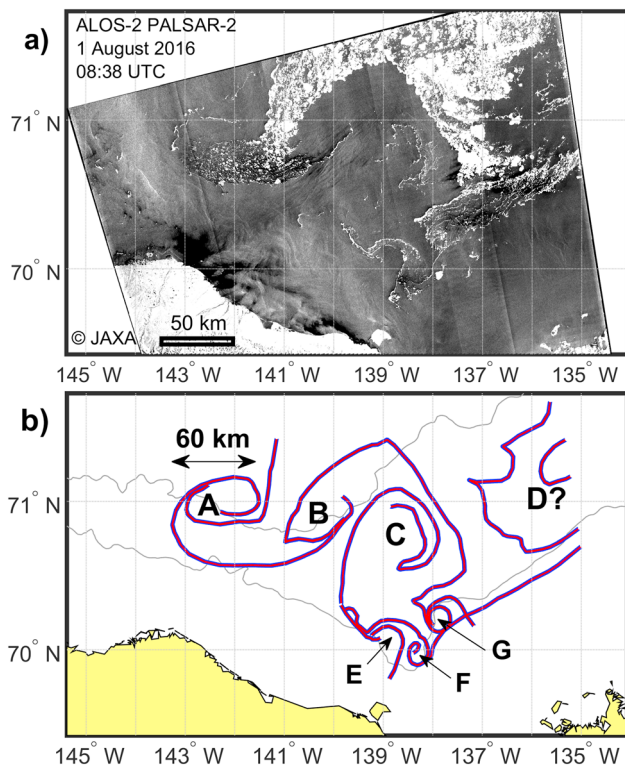
Figure 11. Example of a system of elongated ice tongues with large eddy dipoles observed in the southern Beaufort Sea. (a) Fragment of ALOS-2 Palsar-2 image acquired on 1 August 2016 and (b) its schematic interpretation showing eddy features observed in floating ice fields with color lines drawn along ice boundaries. Letters A–G denote separate eddies observed in the SAR image. Overlaid are bathymetry contours of 200 and 2,000 m.

both for OW and MIZ eddies, the mean diameter of anticyclones is slightly larger compared to cyclones (see example in Figure 11).

Figure 10 further shows a spatial distribution of the mean and the maximum eddy diameters for OW and MIZ eddies. For OW eddies, characteristic eddy diameters of around 5–6 km clearly prevail both over shelf regions and in deep water (Figure 10a). When looking to the mean values over a grid cell, larger eddies of 15–20 km in diameter are often observed over the shelf break and continental slope, as well as over deep water northeast from the Chukchi Plateau. However, when one looks to the maximum value of eddy diameter encountered in the grid cell (Figure 10b), diameters of 10 km become dominating, and much larger eddies with diameters of 20–40 km (up to 60 km) are seen along the southern Beaufort Sea, north-west from Point Barrow, and south of Banks Island. A spatial mean value of a standard deviation for OW eddy diameters is equal to about 4 km.

For MIZ eddies, mean values of 6–10 km dominate over the study site (Figure 10c). Mean diameters of 20–40 km are observed in the central part and over the northern periphery of the Beaufort Gyre, over the shelf break regions in the Beaufort and Chukchi Seas, and between the Mendeleev Ridge and the Chukchi Plateau. The map of maximum diameters of MIZ eddies (Figure 10d) shows that larger eddies of 20–40 km in diameter are present practically everywhere but are more prevalent over depths exceeding 2,000 m. A spatial mean value for maximum eddy diameters shown in Figure 10d is equal to 15 km. For a given grid cell, diameter values of MIZ eddies on average span within 10–11 km with a standard deviation equal to 5.3 km.

An example of large MIZ eddies formed at ice-ocean boundary during a melting season is shown in Figure 11. ALOS-2 Palsar-2 image acquired over the southern Beaufort Sea on 1 August 2016 shows a system of two elongated ice tongues with large eddy dipoles at the end of each. Figure 11b shows a schematic interpretation of eddy features seen in floating ice fields in Figure 11a with color lines drawn along ice boundaries. Manifestations of six eddies are clearly observed in this SAR image. As seen, most of them form eddy dipoles with anticyclones being usually larger than cyclones. This is well seen for the pair A-B, where the diameter of eddy **A** is about 60 km while the adjacent cyclone **B** is about 40 km in diameter. Notably, this system of large eddies is found rather close to the coast but is bounded by 200-m isobath.

4. Summary and Discussion

Using a large data set of multimission spaceborne SAR observations of eddy signatures over the open ocean and in the marginal ice zones, we have developed the first estimate of eddy characteristics spanning the Western Arctic Ocean. Altogether 7,749 SAR manifestations of eddies were identified from June to October in 2007, 2011, and 2016 with 4,078 eddies detected in the open-water regions, and 3,671 eddies—in the marginal ice zone and near the ice edge.

The most prominent feature of the obtained results is that cyclonic eddies strongly dominate over anticyclones in the record: on average there are about 65–70% of cyclonic eddies versus 30–35% of anticyclones. A large portion of eddies is also observed in the form of mushroom-like vortex pairs, consistent with baroclinic instability mechanism (Hogg & Stommel, 1985; Manucharyan & Timmermans, 2014). Such an asymmetry was also observed in previous satellite investigations (see, e.g., Munk et al., 2000; DiGiacomo & Holt, 2001). Further, it was also found in high-resolution numerical simulations revealing strong submesoscale turbulence (e.g., Capet et al., 2008; Mahadevan & Tandon, 2006). Specialized experiments of Roullet and Klein (2010) and Shcherbina et al. (2013) point out that stronger eddies with $|\zeta| = O(f)$, where ζ is the relative vorticity and f is the Coriolis parameter, are expected to be predominantly cyclonic because flows with strong anticyclonic vorticity $\zeta < -f$ are unstable, and flows with strong

cyclonic vorticity are not. Higher number of cyclones observed in satellite data may be also related to their generation by/interaction with anticyclones. As observed in laboratory experiments (Elkin & Zatsepin, 2014), small cyclones are often attached to one larger anticyclone, because anticyclonic horizontal shear is more effective in generation of small submesoscale cyclones than cyclonic shear in generation of small anticyclones (McWilliams, 2016).

The highest total number of open-water eddies is detected in August and September when the region has a minimum ice cover extent. This has some difference with the results obtained for Eurasian Arctic Seas where a peak of eddy detections was observed in July (Atadzhanova et al., 2017). However, the normalized yearly-mean numbers show maximum eddy activity in August and October, while giving nearly similar results for July and August. The maximum occurrence of MIZ eddies is recorded in September and October when the marginal ice zone is well developed and spans 5–7° of latitude. As obtained, the number of eddy detections in the MIZ and along the ice edge is inversely proportional to the background sea ice concentration with more eddies detected over less ice-covered waters.

The range of open-water eddy diameters spans from 0.5 to 61 km. However, diameter values of about 94% of OW eddies do not exceed 10 km with a mean value of 4.7 km. MIZ eddies are usually larger in size with a mean diameter of about 7 km and a wider range of diameters, 0.3–106 km. As observed both for OW and MIZ eddies, the mean diameter of anticyclones is usually somewhat larger than that of cyclones. Similar results showing that mesoscale anticyclones are more long-lived, intense, and larger than cyclones were also obtained for the global ocean (Chelton et al., 2011) and over its different regions (Kang & Curchitser, 2013; Kubryakov & Stanichny, 2015). One of the possible reasons of this asymmetry is related to the difference in the local radius of deformation for eddies of different sign, which is higher for anticyclones compared to cyclones (see D'Hieres et al., 1989; Nezlin & Sutyrin, 1989). Moreover, the smaller sizes of the cyclones may point to them being surface-amplified features that are not extending as deeply as the anticyclones.

Interannual variability in the number of observed eddies is clearly present, with both open ocean and MIZ eddies appearing more frequently in 2016, compared to 2007 and 2011. The observed interannual variability is in line with broad changes of FWC in the Beaufort Gyre during the last decade (Krishfield et al., 2014) where eddies are known to play an important role in buoyancy and freshwater budgets (Manucharyan & Spall, 2016; Meneghello et al., 2017). It has been hypothesized that eddies contribute to the Beaufort Gyre equilibration and hence a more energetic gyre (with higher FWC) must generate a more energetic eddy field (Manucharyan & Spall, 2016). However, the temporal extent of our data set (only three years) does not allow to make a solid conclusion about the link between the BG intensity and the amount of the observed eddies. Potentially, satellite observations from a longer time period could address this question in detail.

As already mentioned, the human supervised method of eddy detection in SAR images could contain various biases. Moreover, given that imaging capabilities of SAR sensors allow to detect eddy signatures mostly under low to moderate winds, and the study site is characterized by relatively strong winds even in summer months, eddy numbers presented in this work should be treated as a lower boundary of a real picture. Moreover, in this work we do not address any aspects of eddy dynamics, including their velocities, lifetimes, and propagation trajectories. This might be improved in the future by considering time sequences of currently operating SAR instruments, or in pair with satellite altimetry observations. Nonetheless, over the course of only a few years of publicly available satellite observations, we have identified an order of magnitude more eddies than what was observed at depth by in situ instruments such as moorings and ice-tethered profilers.

Our observations of eddy characteristics based on their surface signatures are distinct from subsurface eddy characteristics obtained by in situ observations in several ways. We demonstrate that the number of SAR-inferred cyclonic eddies dominate the number of anticyclones at the surface, which is contrary to the in situ observations of a clear dominance of anticyclones below the mixed layer. Also, we identified a much wider range of surface eddy sizes including eddies of only a 0.50 and up to 40–60 km, whereas subsurface eddies were observed to have a much narrower size range of about 10 to 20 km. These differences between the surface and subsurface eddies in their observation frequency, characteristic sizes, and preferred direction of rotation could be caused by a combination of several factors: the lack of spatial coverage by in situ instruments, potential biases in human supervised eddy detection method from SAR images, and distinct eddy formation and dissipation mechanisms.

Indications about potential eddy formation mechanisms could be inferred from their geographic location, sizes, or preferred cyclonicity. While eddies are frequently observed near bathymetric features such as continental shelfs, slopes, and over the Chukchi Plateau, they are also strongly present in the deep Canada Basin within the Beaufort Gyre. Eddies in deep basin are slightly larger in size which may imply that they either have been generated at the boundary currents and advected into the interior of the Beaufort Gyre (Spall et al., 2008) while experiencing inverse energy cascade (Charney, 1971), or generated via baroclinic instabilities of the gyre itself (Manucharyan & Spall, 2016). The analysis of SAR snapshots does not allow to determine eddy vorticity, and hence, it is not possible to explicitly separate mesoscale eddies, which ought to have subsurface signatures, from submesoscale eddies which are surface amplified and likely do not penetrate significantly below the mixed layer. Nonetheless, since the first baroclinic Rossby deformation radii in deep Arctic basins range between 10 and 20 km (Nurser & Bacon, 2014), the eddies with sizes of less than 10 km are likely associated with mixed layer processes such as instabilities of wind- and buoyancy-driven lateral mixed layer gradients (Thomas et al., 2008). Thus, these smaller eddies are likely surface-amplified and would not be detected by ITPs or moorings. Furthermore, if eddies are formed due to instabilities of outcropping surface fronts, then cyclonic (high potential vorticity) eddies must be dominant at the surface while anticyclonic (low potential vorticity) eddies must be more frequent at depth (Manucharyan & Timmermans, 2014), reconciling the seemingly contradictory conclusions about the cyclonicity of eddies.

In this context, more detailed modeling and observational intercomparison studies are necessary to understand the nature of eddy formation and dissipation mechanisms, their role in the interactions with mean currents, and their cumulative transport of water masses and biogeochemical tracers.

References

Abraham, E. R., Law, C. S., Boyd, P. W., Lavender, S. J., Maldonado, M. T., & Bowie, A. R. (2000). Importance of stirring in the development of an iron-fertilized phytoplankton bloom. *Nature*, *407*(6805), 727–730. https://doi.org/10.1038/35037555

Aleskerova, A. A., Kubryakov, A. A., & Stanichny, S. V. (2017). A two-channel method for retrieval of the Black Sea surface temperature from Landsat-8 measurement. *Izvestiya, Atmospheric and Oceanic Physics*, *52*(9), 1155–1161. https://doi.org/10.1134/S0001433816090048

Arbic, B. K., Polzin, K. L., Scott, R. B., Richman, J. G., & Shriver, J. F. (2013). On eddy viscosity, energy cascades, and the horizontal resolution of gridded satellite altimeter products. *Journal of Physical Oceanography*, *43*(2), 283–300. https://doi.org/10.1175/JPO-D-11-0240.1

Armitage, T. W. K., Bacon, S., Ridout, A. L., Petty, A. A., Wolbach, S., & Tsamados, M. (2016). Arctic Ocean surface geostrophic circulation 2003–2014. *The Cryosphere*, *11*(4), 1767–1780. https://doi.org/10.5194/tc-11-1767-2017

Atadzhanova, O. A., Zimin, A. V., Romanenkov, D. A., & Kozlov, I. E. (2017). Satellite radar observations of small eddies in the White, Barents and Kara Seas. *Physical Oceanography*, *2*(2), 75–83. https://doi.org/10.22449/1573-160X-2017-2-75-83

Capet, X., McWilliams, J. C., Molemaker, M. J., & Shchepetkin, A. F. (2008). Mesoscale to submesoscale transition in the California current system. Part I: Flow structure, eddy flux, and observational tests. *Journal of Physical Oceanography*, *38*(10), 2256–2269. https://doi.org/10.1175/2008JPO3810.1

Charney, J. G. (1971). Geostrophic turbulence. *Journal of the Atmospheric Sciences*, *37*(10), 2394–2414. https://doi.org/10.1080/01431161.2016.1145367

Chelton, D. B., Schlax, M. G., & Samelson, R. M. (2011). Global observations of nonlinear mesoscale eddies. *Progress in Oceanography*, *91*(2), 167–216. https://doi.org/10.1016/j.pocean.2011.01.002

D'Asaro, E. (1988). Observations of small eddies in the Beaufort Sea. *Journal of Geophysical Research*, *93*(C6), 6669–6684. https://doi.org/10.1029/JC093iC06p06669

D'Hieres, G. C., Davies, P. A., & Didelle, H. (1989). Laboratory studies of pseudo-periodic forcing due to vortex shedding from an isolated solid obstacle in a homogeneous rotating fluid. *Elsevier Oceanography Series*, *50*, 639–653. https://doi.org/10.1016/S0422-9894(08)70212-5

DiGiacomo, P. M., & Holt, B. (2001). Satellite observations of small coastal ocean eddies in the Southern California Bight. *Journal of Geophysical Research*, *106*(C10), 22,521–22,543. https://doi.org/10.1029/2000JC000728

Dokken, S. T., & Wahl, T. (1996). Observations of spiral eddies along the Norwegian coast in ERS SAR images. Norwegian Defence Research Establishment (NDRE), Rep. 96/01463, 29 p. https://doi.org/10.1029/2005JC003384

Eldevik, T., & Dysthe, K. B. (2002). Spiral eddies. *Journal of Physical Oceanography*, *32*(3), 851–869. https://doi.org/10.1175/1520-0485(2002)032<0851:SE>2.0.CO;2

Elkin, D. N., & Zatsepin, A. G. (2014). Laboratory study of a shear instability of an alongshore sea current. *Oceanology*, *54*(5), 576–582. https://doi.org/10.1134/s000143701405004x

Fine, E. C., MacKinnon, J. A., Alford, M. H., & Mickett, J. B. (2018). Microstructure observations of turbulent heat fluxes in a warm-core Canada Basin eddy. *Journal of Physical Oceanography*, *48*(10), 2397–2418. https://doi.org/10.1175/jpo-d-18-0028.1

Hattermann, T., Isachsen, P. E., Von Appen, W.-J., Albretsen, J., & Sundfjord, A. (2016). Eddy-driven recirculation of Atlantic Water in Fram Strait. *Geophysical Research Letters*, *43*, 3406–3414. https://doi.org/10.1002/2016GL068323

Hogg, N. G., & Stommel, H. M. (1985). The heton, an elementary interaction between discrete baroclinic geostrophic vortices, and its implications concerning eddy heat-flow. Proceedings of the Royal Society of London. *A Mathematical and Physical Sciences*, *397*(1812), 1–20. https://doi.org/10.1098/rspa.1985.0001

Hunkins, K. L. (1974). Subsurface eddies in the Arctic Ocean. *Deep Sea Research and Oceanographic Abstracts*, *21*(12), 1017–1033. https://doi.org/10.1016/0011-7471(74)90064-3

Jakobsson, M., Mayer, L., Coakley, B., Dowdeswell, J. A., Forbes, B. S., & Fridman, et al. (2012). The International Bathymetric Chart of the Arctic Ocean (IBCAO) version 3.0. *Geophysical Research Letters*, *39*, L12609. https://doi.org/10.1029/2012GL052219

Johannessen, J. A., Kudryavtsev, V., Akimov, D., Eldevik, T., Winther, N., & Chapron, B. (2005). On radar imaging of current features: 2. Mesoscale eddy and current front detection. *Journal of Geophysical Research*, *110*, C07017. https://doi.org/10.1029/2004JC002802

Johannessen, J. A., Reed, L. P., & Wahl, T. (1993). Eddies detected in ERS-1 SAR images and simulated in reduced gravity model. *International Journal of Remote Sensing*, *14*(11), 2203–2213. https://doi.org/10.1080/01431169308954029

Johannessen, J. A., Shuchman, R. A., Digranes, G., Lyzenga, D. R., Wackerman, C., Johannessen, O. M., & Vachon, P. W. (1996). Coastal ocean fronts and eddies imaged with ERS 1 synthetic aperture radar. *Journal of Geophysical Research*, *101*(C3), 6651–6667. https://doi.org/10.1029/95JC02962

Johannessen, O. M., Johannessen, J. A., Svendsen, E., Shuchman, R. A., Campbell, W. J., & Josberger, E. (1987). Ice-edge eddies in the Fram Strait marginal ice zone. *Science*, *236*(4800), 427–429. https://doi.org/10.1126/science.236.4800.427

Kang, D., & Curchitser, E. N. (2013). Gulf Stream eddy characteristics in a high-resolution ocean model. *Journal of Geophysical Research: Oceans*, *118*, 4474–4487. https://doi.org/10.1002/jgrc.20318

Karimova, S. S. (2012). Spiral eddies in the Baltic, Black and Caspian Seas as seen by satellite radar data. *Advances in Space Research*, *50*(8), 1107–1124. https://doi.org/10.1016/j.asr.2011.10.027

Karimova, S. S., & Gade, M. (2016). Improved statistics of sub-mesoscale eddies in the Baltic Sea retrieved from SAR imagery. *International Journal of Remote Sensing*, *37*(10), 2394–2414. https://doi.org/10.1080/01431161.2016.1145367

Kozlov, I. E., Kudryavtsev, V. N., Johannessen, J. A., Chapron, B., Dailidiene, I., & Myasoedov, A. G. (2012). ASAR imaging for coastal upwelling in the Baltic Sea. *Advances in Space Research*, *50*(8), 1125–1137. https://doi.org/10.1016/j.asr.2011.08.017

Kozlov, I. E., Kudryavtsev, V. N., Zubkova, E. V., Zimin, A. V., & Chapron, B. (2015). Characteristics of short-period internal waves in the Kara Sea inferred from satellite SAR data. *Izvestiya, Atmospheric and Oceanic Physics*, *51*(9), 1073–1087. https://doi.org/10.1134/S0001433815090121

Krishfield, R. A., Proshutinsky, A., Tateyama, K., Williams, W. J., Carmack, E. C., McLaughlin, F. A., & Timmermans, M.-L. (2014). Deterioration of perennial sea ice in the Beaufort Gyre from 2003 to 2012 and its impact on the oceanic freshwater cycle. *Journal of Geophysical Research: Oceans*, *119*, 1271–1305. https://doi.org/10.1002/2013JC008999

Kubryakov, A., & Stanichny, S. V. (2015). Mesoscale eddies in the Black Sea from satellite altimetry data. *Oceanology*, *55*(1), 56–67. https://doi.org/10.1134/S0001437015010105

Kudryavtsev, V., Kozlov, I., Chapron, B., & Johannessen, J. A. (2014). Quad-polarization SAR features of ocean currents. *Journal of Geophysical Research: Oceans*, *119*, 6046–6065. https://doi.org/10.1002/2014JC010173

Lee, J.-S. (1983). Digital image smoothing and the sigma filter. *Computer Vision, Graphics, and Image Processing*, *24*(2), 255–269. https://doi.org/10.1016/0734-189X(83)90047-6

Lim, J. S. (1990). *Two-dimensional signal and image processing*. Englewood Cliffs, NJ: Prentice Hall.

Lu, K. (2015). Lateral mixing across ice meltwater fronts of the Chukchi Sea shelf. *Geophysical Research Letters*, *42*, 6754–6761. https://doi.org/10.1002/2015GL064967

Mahadevan, A., & Tandon, A. (2006). An analysis of mechanisms for submesoscale vertical motion at ocean fronts. *Ocean Modell*, *14*(3-4), 241–256. https://doi.org/10.1016/j.ocemod.2006.05.006

Manley, T. O., & Hunkins, K. (1985). Mesoscale eddies of the Arctic Ocean. *Journal of Geophysical Research*, *90*(C3), 4911–4930. https://doi.org/10.1029/JC090iC03p04911

Manucharyan, G. E., & Spall, M. A. (2016). Wind-driven freshwater buildup and release in the Beaufort Gyre constrained by mesoscale eddies. *Geophysical Research Letters*, *43*, 273–282. https://doi.org/10.1002/2015GL065957

Manucharyan, G. E., Spall, M. A., & Thompson, A. F. (2016). A theory of the wind-driven Beaufort Gyre variability. *Journal of Physical Oceanography*, *46*, 3263–3278. https://doi.org/10.1175/JPO-D-16-0091.1

Manucharyan, G. E., & Thompson, A. F. (2017). Submesoscale sea ice-ocean interactions in marginal ice zones. *Journal of Geophysical Research: Oceans*, *122*, 9455–9475. https://doi.org/10.1002/2017JC012895

Manucharyan, G. E., & Timmermans, M.-L. (2014). Generation and separation of mesoscale eddies from surface ocean fronts. *Journal of Physical Oceanography*, *43*(12), 2545–2562. https://doi.org/10.1175/JPO-D-13-094.1

McWilliams, J. C. (2016). Submesoscale currents in the ocean. *Proceedings of the Royal Society A.*, *472*(2189). https://doi.org/10.1098/rspa.2016.0117

Meneghello, G., Marshall, J., Cole, S. T., & Timmermans, M.-L. (2017). Observational inferences of lateral eddy diffusivity in the halocline of the Beaufort Gyre. *Geophysical Research Letters*, *44*, 12,331–12,338. https://doi.org/10.1002/2017GL075126

Mensa, J. A., Timmermans, M.-L., Kozlov, I. E., Williams, W. J., & Özgökmen, T. (2018). Surface drifter observations from the Arctic Ocean's Beaufort Sea: Evidence for submesoscale dynamics. *Journal of Geophysical Research: Oceans*, *123*, 2635–2645. https://doi.org/10.1002/2017JC013728

Muench, R. D., Gunn, J. T., Whitledge, T. E., Schlosser, P., & Smethie, W. (2000). An Arctic Ocean cold core eddy. *Journal of Geophysical Research*, *105*(C10), 23,997–24,006. https://doi.org/10.1029/2000JC000212

Munk, W., Armi, L., Fischer, K., & Zachariasen, F. (2000). Spirals on the sea. *Proceedings of the Royal Society of London. Series A: Mathematical, Physical and Engineering Sciences*, *456*(1997), 1217–1280. https://doi.org/10.1098/rspa.2000.0560

Nezlin, M. V., & Sutyrin, G. G. (1989). Long-lived solitary anticyclones in the planetary atmospheres and oceans, in Laboratory experiments and in theory. *Elsevier Oceanography Series*, *50*, 701–719. https://doi.org/10.1016/S0422-9894(08)70216-2

Niebauer, H. J., & Smith, O. W. Jr. (1989). A numerical model of mesoscale physical-biological interactions in the Fram Strait marginal ice zone. *Journal of Geophysical Research*, *94*(C11), 16,151–16,175. https://doi.org/10.1029/JC094iC11p16151

Nurser, A. J. G., & Bacon, S. (2014). The Rossby radius in the Arctic Ocean. *Ocean Science*, *124*(2), 844–862. https://doi.org/10.1029/2018JC014379

Padman, L., Levine, M., Dillon, T., Morison, J., & Pinkel, R. (1990). Hydrography and microstructure of an Arctic cyclonic eddy. *Journal of Geophysical Research*, *95*(C6), 9411–9719. https://doi.org/10.1029/JC095iC06p09411

Pickart, R. S. (2004). Subsurface eddies in the Arctic Ocean. *Journal of Geophysical Research*, *109*, C04024. https://doi.org/10.1029/2003JC001912

Rocha, C. B., Chereskin, T. K., Gille, S. T., & Menemenlis, D. (2016). Mesoscale to submesoscale wavenumber spectra in Drake Passage. *Journal of Physical Oceanography*, *46*(2), 601–620. https://doi.org/10.1175/jpo-d-15-0087.1

Roullet, G., & Klein, P. (2010). Cyclone-Anticyclone Asymmetry in Geophysical Turbulence. *Physical Review Letters*, *104*(21). https://doi.org/10.1103/physrevlett.104.218501

Shcherbina, A. Y., D'Asaro, E. A., Lee, C. M., Klymak, J. M., Molemaker, M. J., & McWilliams, J. C. (2013). Statistics of vertical vorticity, divergence, and strain in a developed submesoscale turbulence field. *Geophysical Research Letters*, *40*, 4706–4711. https://doi.org/10.1002/grl.50919

Shuchman, R. A., Johannessen, O. M., Campbell, W. J., Lannelongue, N., Burns, B. A., Josberger, E. G., & Manley, T. (1987). Remote sensing of the Fram Strait marginal ice zone. *Science*, *236*(4800), 429–431. https://doi.org/10.1126/science.236.4800.429

Spall, M., Pickart, R., Fratantoni, P., & Plueddemann, A. (2008). Western Arctic shelfbreak eddies: Formation and transport. *Journal of Physical Oceanography*, *38*(8), 1644–1668. https://doi.org/10.1175/2007JPO3829.1

Spreen, G., Kaleschke, L., & Heygster, G. (2008). Sea ice remote sensing using AMSR-E 89 GHz channels. *Journal of Geophysical Research*, *113*, C02S03. https://doi.org/10.1029/2005JC003384

Su, Z., Wang, J., Klein, P., Thompson, A. F., & Menemenlis, D. (2018). Ocean submesoscales as a key component of the global heat budget. *Nature Communications*, *9*(1), 1–8. https://doi.org/10.1038/s41467-018-02983-w

Thomas, L. N., Tandon, A., & Mahadevan, A. (2008). Submesoscale processes and dynamics. *Geophysical Monograph Series*, 17–38. https://doi.org/10.1029/177gm04

Timmermans, M.-L., Toole, J., Proshutinsky, A., Krishfield, R., & Plueddemann, A. (2008). Eddies in the Canada Basin, Arctic Ocean, observed from ice-tethered profilers. *Journal of Physical Oceanography*, *38*(1), 133–145. https://doi.org/10.1175/2007JPO3782.1

Von Appen, W.-J., Wekerle, C., Hehemann, L., Schourup-Kristensen, V., Konrad, C., & Iversen, M. H. (2018). Observations of a submesoscale cyclonic filament in the marginal ice zone. *Geophysical Research Letters*, *45*, 6141–6149. https://doi.org/10.1029/2018GL077897

Watanabe, E., Onodera, J., Harada, N., Honda, M. C., Kimoto, K., Kikuchi, T., et al. (2014). Enhanced role of eddies in the Arctic marine biological pump. *Nature Communications*, *5*(1), 3950. https://doi.org/10.1038/ncomms4950

Wekerle, C., Wang, Q., Von Appen, W.-J., Danilov, S., Schourup-Kristensen, V., & Jung, T. (2017). Eddy-resolving simulation of the Atlantic water circulation in the Fram Strait with focus on the seasonal cycle. *Journal of Geophysical Research: Oceans*, *122*, 8385–8405. https://doi.org/10.1002/2017JC012974

Wunsch, C., & Stammer, D. (1998). Satellite altimetry, the marine geoid, and the oceanic general circulation. *Annual Review of Earth and Planetary Sciences*, *26*(1), 219–253. https://doi.org/10.1146/annurev.earth.26.1.219

Zhao, M., & Timmermans, M.-L. (2015). Vertical scales and dynamics of eddies in the Arctic Ocean's Canada Basin. *Journal of Geophysical Research: Oceans*, *120*, 8195–8209. https://doi.org/10.1002/2015JC011251

Zhao, M., Timmermans, M.-L., Cole, S., Krishfield, R., & Manucharyan, G. E. (2018). Partitioning of kinetic energy in the Arctic Ocean's Beaufort Gyre. *Journal of Geophysical Research: Oceans*, *123*, 4806–4819. https://doi.org/10.1029/2018JC014037

Zhao, M., Timmermans, M.-L., Cole, S., Krishfield, R., Proshutinsky, A., & Toole, J. (2014). Characterizing the eddy field in the Arctic Ocean halocline. *Journal of Geophysical Research: Oceans*, *109*, 8800–8817. https://doi.org/10.1029/2003JC001912

Zhao, M., Timmermans, M.-L., Cole, S., Krishfield, R., & Toole, J. (2016). Evolution of the eddy field in the Arctic Ocean's Canada Basin, 2005–2015. *Geophysical Research Letters*, *43*, 8106–8114. https://doi.org/10.1002/2016GL069671